

From Biomass to Functional Crystalline Diamond Nanothread: Pressure-Induced Polymerization of 2,5-Furandicarboxylic Acid

Xuan Wang, Xin Yang, Yida Wang, Xingyu Tang, Haiyan Zheng, Peijie Zhang, Dexiang Gao, Guangwei Che, Zijia Wang, Aijiao Guan, Jun-Feng Xiang, Mingxue Tang, Xiao Dong, Kuo Li,* and Ho-kwang Mao

HPSTAR
1421-2022



Cite This: *J. Am. Chem. Soc.* 2022, 144, 21837–21842



Read Online

ACCESS |



Metrics & More



Article Recommendations



Supporting Information

ABSTRACT: 2,5-Furandicarboxylic acid (FDCA) is one of the top-12 value-added chemicals from sugar. Besides the wide application in chemical industry, here we found that solid FDCA polymerized to form an atomic-scale ordered sp^3 -carbon nanothread (CNT_h) upon compression. With the help of perfectly aligned π - π stacked molecules and strong intermolecular hydrogen bonds, crystalline poly-FDCA CNT_h with uniform *syn*-configuration was obtained above 11 GPa, with the crystal structure determined by Rietveld refinement of the X-ray diffraction (XRD). The in situ XRD and theoretical simulation results show that the FDCA experienced continuous [4 + 2] Diels–Alder reactions along the stacking direction at the threshold C...C distance of ~ 2.8 Å. Benefiting from the abundant carbonyl groups, the poly-FDCA shows a high specific capacity of 375 mAh g⁻¹ as an anode material of a lithium battery with excellent Coulombic efficiency and rate performance. This is the first time a three-dimensional crystalline CNT_h is obtained, and we demonstrated it is the hydrogen bonds that lead to the formation of the crystalline material with a unique configuration. It also provides a new method to move biomass compounds toward advanced functional carbon materials.

Production of green polymeric materials from biomass-based platform chemicals is necessary for a sustainable and greener society.^{1–4} 2,5-Furandicarboxylic acid (FDCA) is a well-known renewable building block that can be synthesized from oxidation of 5-hydroxymethylfurfural (HMF, an intermediate product of the acid dehydration of sugars) or directly from carbohydrates by a one-pot reaction.^{5,6} It has two carboxyl groups and can be transformed into several families of useful compounds, like the polyesters, polyurethanes, and polyamides.^{7–10} On the other hand, the furan ring is also an important precursor for constructing advanced materials. Very recently, furan was reported to transfer into sp^3 -carbon nanothreads (CNT_hs) via a pressure-induced polymerization (PIP) process under a relatively low pressure (~ 10 GPa) due to its reduced aromaticity, and a large-scale synthesis can thus be achieved.^{11,12} Such CNT_hs were also called diamond nanothreads,^{13–19} which were predicted to have extraordinary high tensile strength and bending modulus and have potential application in tunable thermal conductivity materials, energy storage devices, and nanoelectromechanical systems.^{20–22} Comparing to benzene,^{13–15} the furan ring has only four carbon atoms, resulting in fewer possible bonding routes and hence improving the homogeneity of the CNT_hs.²³ Under the help of the advanced solid-state nuclear magnetic resonance (NMR) techniques, Matsuura et al. concluded that about 10% of the sample is a perfect furan-CNT_h, with an almost entirely *anti*-configuration.¹² Besides, the stacking order and intermolecular interaction (π - π stacking^{24–27} and H-bonding^{28–30}) of reactant molecules were also key factors in the preparation of structure-specific crystalline polymeric material, as evidenced by the PIP product of the naphthalene–

octafluoronaphthalene cocrystal,^{24,25} *s*-triazine,²⁶ pyridazine,²⁷ aniline,²⁸ acetylenedicarboxylic acid,²⁹ etc. Therefore, with the two pairs of intercarboxyl H-bonds, FDCA should be a better precursor for the synthesis of crystalline structure-specific CNT_hs. In this work, by compressing FDCA we obtained crystalline, carboxyl-substituted *syn*-furan-CNT_hs, as determined by the Rietveld refinement of X-ray diffraction (XRD) data, in obvious contrast to the furan-derived CNT_hs with *anti*-configuration.^{11,12} The carboxyl and the CNT_h skeleton result in a good electrochemical performance and chemical stability for application as lithium-ion battery (LIB) anode material. Our work demonstrated a direct high-pressure synthetic route from biomass to advanced functional carbon-based material with excellent electrochemical properties and unique mechanical merit.

At ambient pressure, FDCA has a monoclinic lattice (Figure 1, space group $P2_1/m$) with $a = 4.97(1)$ Å, $b = 16.69(2)$ Å, $c = 3.66(1)$ Å, and $\beta = 96(1)^\circ$.³¹ The furan rings are stacked into columns with *syn*-configuration (all the oxygens on one side) along the c -axis, and these columns are connected by H-bonds along the b -axis. The angle between the furan plane and the a - b plane is 33.8° , and the minimum intermolecular distance between carbon atoms is $d_{C_2\dots C_3'} = 3.284$ Å. We investigated the high-pressure structural evolution of FDCA by in situ

Received: August 21, 2022

Published: November 18, 2022



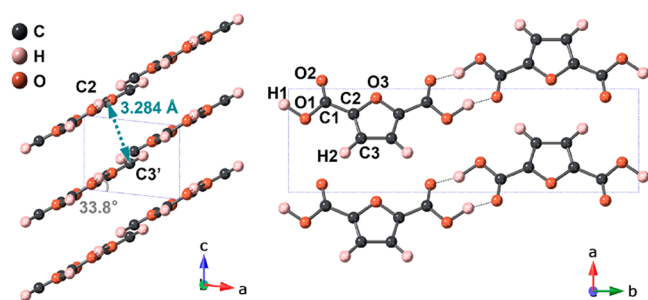


Figure 1. Crystal structure of FDCA at ambient pressure viewed along the *b*- and *c*-axis.

synchrotron XRD experiments (Figures 2a and S1). Upon compression, the diffraction peaks moved toward higher angles. It is worth noting that the peak 020 (index below the patterns in Figure 2a, at $\sim 4.3^\circ$) moved only a little bit, suggesting the structural stability of the *b*-axis (the direction of the H-bond). The 001 and -101 peaks moved the fastest, indicating the most pronounced deformation along the furan column. The cell parameters and volume of FDCA at high pressures were obtained by Le Bail fitting of the XRD data, which demonstrated the anisotropic compression quantitatively (Figure S2). At 12.1 GPa, new diffraction peaks appeared at 8.0° and 11.7° (marked by asterisks in Figure 2a), close to the peaks 110 and 140, respectively, and the sample became brown (Figure S3), which indicates the onset of reaction and the generation of poly-FDCA. These peaks were maintained at higher pressure and during decompression, and a series of diffraction peaks including $d = 8.45, 5.18, 4.96,$ and 3.25 \AA were clearly observed after decompression to 1.0 GPa.

The critical crystal structure of FDCA at 10.8 GPa (just before reaction, Figure 2b) was determined by Le Bail fitting

and subsequent density functional theory (DFT) optimization of the atomic coordinates. The FDCA molecule maintained in plane, and the $d_{C2...C3'}$ between adjacent furan rings was compressed to 2.788 \AA (green line in Figure 2b). This distance agrees with the reaction threshold ($d_{C...C}$) of many aromatic molecules under high pressure, like $d_{C...C} = 2.8 \text{ \AA}$ for benzene³² and $C_6H_6-C_6F_6$ cocrystals,³³ and hence suggests that FDCA can polymerize via a $[4 + 2]$ cycloaddition reaction by bonding of $C2...C3'$, as confirmed by the solid-state NMR studies of the furan-CNTh.¹² Our dynamic simulation result also followed this route and produced the *syn*-FDCA-CNTh as expected (Figure S4).

To investigate the crystal structure of the poly-FDCA experimentally, we synthesized milligrams of the polymerized product by Paris–Edinburgh (PE) press at 30 GPa (noted as PE-30). Compared to the reported benzene/furan/thiophene-derived CNThs with only one broad diffraction peak at $4.9\text{--}5.6 \text{ \AA}$,^{11,15,18} the poly-FDCA shows many sharp diffractions (Figure 2c and Figure S5 plotted in *d*-spacing) with a minimum *d*-spacing of $\sim 1.4 \text{ \AA}$ distinguished. This unambiguously demonstrated the atomic-level ordering in the CNThs. Inspired by the theoretical simulation, a monoclinic unit cell was used to index the pattern perfectly, and the lattice parameters were obtained with $a = 5.3526(5) \text{ \AA}$, $b = 16.9062(12) \text{ \AA}$, $c = 2.6632(3) \text{ \AA}$, $\alpha = \gamma = 90^\circ$, and $\beta = 90.23(9)^\circ$ by Rietveld refinement (Figures 2c and S5, Table S1). The intense peaks at $8.46, 5.36,$ and 2.66 \AA are indexed as 020, 100, and 001, respectively, indicating that the crystal structure has excellent ordering in three dimensions (3D). The atomic coordinates were also determined by Rietveld refinement (Table S2), forming a *syn*-FDCA-CNTh structure. As shown in Figure 2d, the furan units form *syn*-CNThs along the *c*-axis and the H-bonds connect the CNThs in the *a*–*b* plane

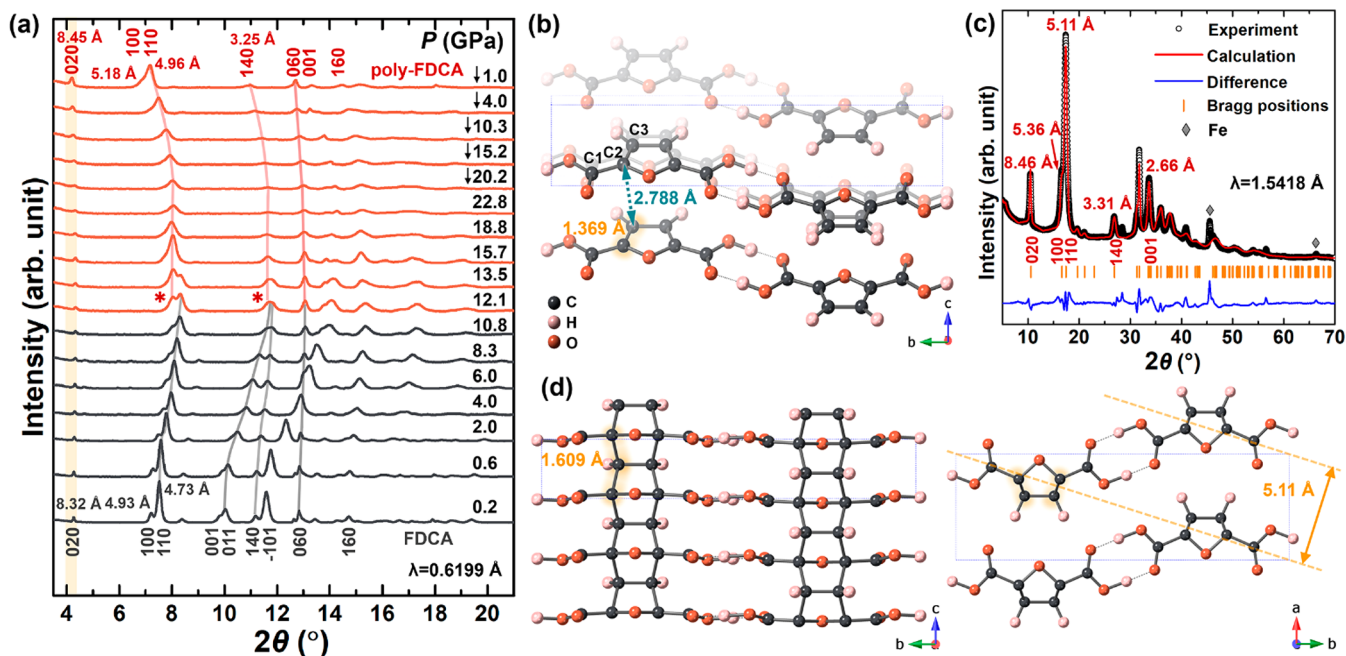


Figure 2. (a) Synchrotron XRD patterns of FDCA at selected pressures. The red asterisks indicate the formation of poly-FDCA, and down-arrows represent decompression. The gray and red lines represent the diffraction peak shifts of FDCA and poly-FDCA, respectively. The Miller indices and the corresponding *d*-spacings of FDCA and poly-FDCA are labeled. (b) The critical crystal structure of FDCA at 10.8 GPa. (c) Rietveld refinement plot of the XRD pattern. The diamond labels represent the diffraction peaks of iron chips from the gasket. (d) Crystal structure of *syn*-FDCA-CNTh.

to form a network as in the reactant, in agreement with the dynamic simulation results mentioned above. This is the first time the atomic-level structure of CNTh was determined due to its enhanced structural ordering. The poly-FDCA has a unique *syn*-configuration and complete interthread ordering, in obvious contrast to the furan-CNThs and other CNThs. This is attributed to the in-phase columnar stacking of the FDCA monomer, which is locked by the H-bonds between carboxyl groups and cannot rotate during the polymerization.

The polymerization process of FDCA was also tracked by the in situ infrared (IR) spectroscopy (Figures 3a and S6a and

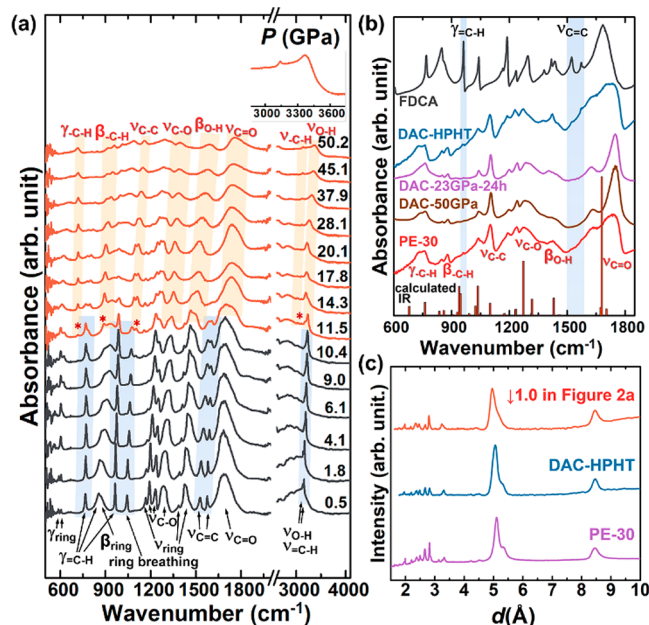


Figure 3. (a) In situ IR spectra of FDCA upon compression. The inset shows the amplified spectrum at 50.2 GPa; the blue and yellow regions mark the characteristic IR peaks of the FDCA and poly-FDCA, respectively. ν , γ , and β represent the stretching, out-of-plane bending, and in-plane bending vibration, respectively. (b) IR spectra collected at ambient pressure and room temperature for FDCA and poly-FDCA synthesized at various conditions, and the calculated IR spectrum of the *syn*-FDCA-CNTh. (c) XRD patterns of DAC-HPHT and PE-30 at ambient pressure and room temperature, with the in situ DAC sample decompressed to 1 GPa for comparison.

(b) with the IR modes assigned in Table S3. Above 11.5 GPa, the characteristic IR modes of the furan ring including the out-of-plane bending of $\text{C}=\text{C}-\text{H}$ ($\gamma_{\text{C}=\text{H}}$, 771, 905, and 987 cm^{-1}) and the stretching vibration of $\text{C}=\text{C}$ ($\nu_{\text{C}=\text{C}}$, 1584 and 1603 cm^{-1}) gradually disappeared. Meanwhile, four new peaks appeared at 716, 889, 1103, and 3106 cm^{-1} , which are assigned to the $\text{C}-\text{H}$ out-of-plane bending mode ($\gamma_{\text{C}-\text{H}}$), $\text{C}-\text{H}$ in-plane bending mode ($\beta_{\text{C}-\text{H}}$), $\text{C}-\text{C}$ stretching mode ($\nu_{\text{C}-\text{C}}$), and $\text{sp}^3\text{-C}-\text{H}$ stretching mode ($\nu_{\text{C}-\text{H}}$), respectively (red asterisks in Figures 3a and S6b). Furthermore, the profiles of the ν -ring and $\text{C}=\text{O}$ stretching ($\nu_{\text{C}=\text{O}}$) modes at 1465 and 1696 cm^{-1} start to change significantly. All of these clearly confirmed the onset of the reaction of FDCA, with the transformation from sp^2 -carbon to sp^3 -carbon. The pressure dependence of selected IR peaks also shows obvious discontinuity or new peaks at 10–12 GPa, demonstrating the PIP clearly (Figure S6c). During decompression (Figure S6d) down to ambient pressure (DAC-50 GPa in Figure 3b), the vibration modes ($\gamma_{\text{C}-\text{H}}$, $\beta_{\text{C}-\text{H}}$, $\nu_{\text{C}-\text{C}}$, $\nu_{\text{C}-\text{H}}$) of poly-FDCA

were maintained, and the $\gamma_{\text{C}=\text{H}}$ and $\nu_{\text{C}=\text{C}}$ modes of FDCA did not reappear, indicating the irreversibility of the reaction and the stability of the CNTh. Moreover, the IR spectra of DAC-50 GPa and PE-30 (Figure 3b) are nearly identical, indicating that the polymers made from DAC and PE press have the same structure. The calculated IR spectrum of *syn*-FDCA-CNTh makes an excellent match to the experimental IR spectrum, which further validates the model (Figure 3b).

The synthetic pressure of poly-FDCA was significantly reduced by increasing the reaction time and temperature, as confirmed by the IR spectra and XRD (Figures 3b,c and S7). The samples obtained using DAC at 50 GPa (DAC-50 GPa), at 23 GPa for 24 h (DAC-23 GPa-24h), at 350 °C and 12 GPa (DAC-HPHT), respectively, and PE-30 have similar IR spectra, and the featured peak of FDCA like $\gamma_{\text{C}=\text{H}}$ and $\nu_{\text{C}=\text{C}}$ (marked in blue in Figure 3b) already disappeared. The XRD data of DAC-HPHT are consistent at different positions, indicating a good homogeneity (Figure S8). The patterns are almost identical to that of PE-30 and can be fitted with the *syn*-FDCA-CNTh model (Figures 3c and S9, Tables S4 and S5). It is worth noting that this is a milder condition for scalable preparation.

The abundant carbonyl groups bring redox properties to poly-FDCA, which provides a binding site for Li^+ ions through reversible electron transfer. We evaluated the electrochemical performance of PE-30 as an LIB anode material by fabricating half-cells. As shown in Figure 4a, the cyclic voltammogram

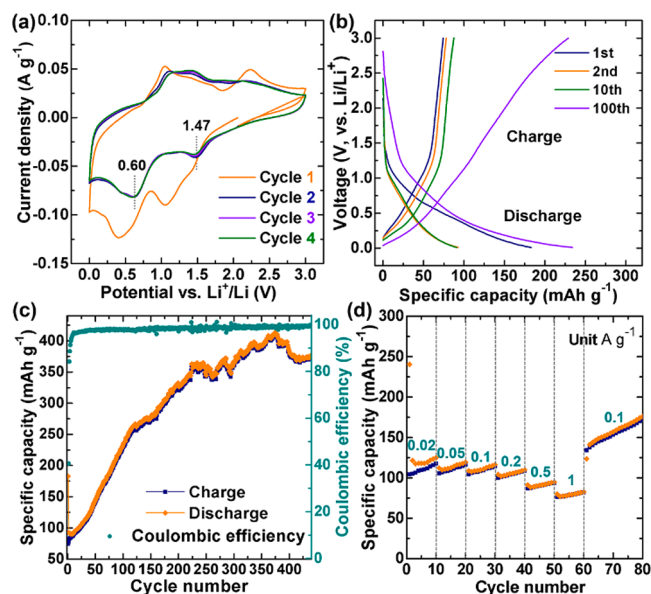


Figure 4. Electrochemical performance of PE-30 as an LIB anode material. (a) CV curves at a scan rate of 0.5 mV s^{-1} . (b) Galvanostatic discharge–charge profiles and (c) electrochemical cycling performance at a current density of 0.1 A g^{-1} . (d) Rate performance under different current densities (A g^{-1}).

(CV) curves show a pronounced reduction peak at 0.41 V in the first cycle, attributed to the formation of a solid electrolyte interface (SEI) film on the surface and the irreversible bonding of Li^+ ions to the carboxyl groups. This is consistent with the first charge–discharge profile shown in Figure 4b, corresponding to a Coulombic efficiency of 40.57%. In the following cycles, two cathodic peaks were steadily observed at ~ 0.60 and ~ 1.47 V owing to the reduction of carbonyl groups upon

insertion of Li⁺ ions. The capacity and Coulombic efficiency increased dramatically upon cycling (Figure 4c), suggesting continuous activation of the poly-FDCA material and reversible insertion of Li⁺ ions. The discharge/charge specific capacity reached a maximum of ~413 mAh g⁻¹ at the 374th cycle and maintained ~375 mAh g⁻¹ with a Coulombic efficiency above 99% in the subsequent cycles. This is close to the capacity of graphite (specific capacity of ~360 mAh g⁻¹ by the formation of LiC₆),³⁴ which is the most commonly used anode material for lithium ions today. By reducing the constant current to 0.1 A g⁻¹ after charging and discharging at a high rate of 1 A g⁻¹ (Figure 4d), the discharge specific capacity was recovered to 141.1 mAh g⁻¹, reflecting good cycle/rate performance and structural stability. These results demonstrated that the poly-FDCA-CNTh is a good candidate as an LIB anode material.

In summary, we synthesized crystalline carboxyl-substituted *syn*-furan-CNTh with uniform chemical structure and excellent electrochemical properties as an LIB anode. The product shows distinct XRD peaks in three dimensions, which allowed determining the atomic positions by Rietveld refinement. The continuous [4 + 2] cycloaddition reactions along the furan columns were concluded based on the structural analysis under threshold pressure and IR spectral evolution. The H-bonds guided the polymerization pathway to obtain the structure-specific crystalline product. The chemical stability of the sp³-CNTh backbone and the high content of carbonyl groups resulted in high electrochemical specific capacity and excellent cycling stability and evidenced that poly-FDCA is a good candidate for the LIB anode materials. This is the first example to show the application of the functionalized diamond nanothreads. Due to their high stiffness, better water affinity, and enhanced intermolecular interaction, more applications like reinforcement for the nanocomposites and development of biocompatible materials can be expected. More importantly, since H-bonds are very common in biomass molecules, and the molecules are often unsaturated, ready for polymerization upon compression, our work actually provides a high-pressure route for tailored synthesis of functional carbon-based materials from biomass.

■ ASSOCIATED CONTENT

SI Supporting Information

The Supporting Information is available free of charge at <https://pubs.acs.org/doi/10.1021/jacs.2c08914>.

Experimental procedures; synchrotron XRD patterns of FDCA under applied pressures; evolution of corresponding compression ratio of lattice parameters; *P*–*V* relationship of FDCA fitted by the third-order Birch–Murnaghan equation of state; optical micrographs of FDCA powder collected at selected pressures; poly-FDCA model obtained by dynamic simulation; XRD pattern of PE-30; IR investigation of FDCA under external pressure; IR spectra collected at ambient pressure and room temperature of the products synthesized at high pressure and room temperature and high pressure and high temperature; XRD data of poly-FDCA synthesized at 12 GPa and 350 °C; Rietveld refinement plot of the XRD pattern of product DAC-HPHT; Rietveld refinement results of PE-30 and DAC-HPHT based on the XRD data; atomic coordinates of

PE-30 and DAC-HPHT; assignments of IR modes of FDCA (PDF)

■ AUTHOR INFORMATION

Corresponding Author

Kuo Li – Center for High Pressure Science and Technology Advanced Research, Beijing 100193, People's Republic of China; orcid.org/0000-0002-4859-6099; Email: likuo@hpstar.ac.cn

Authors

Xuan Wang – Center for High Pressure Science and Technology Advanced Research, Beijing 100193, People's Republic of China; Institute of High Energy Physics, Chinese Academy of Sciences, Beijing 100049, People's Republic of China; orcid.org/0000-0001-6647-9542

Xin Yang – Center for High Pressure Science and Technology Advanced Research, Beijing 100193, People's Republic of China

Yida Wang – Center for High Pressure Science and Technology Advanced Research, Beijing 100193, People's Republic of China

Xingyu Tang – Center for High Pressure Science and Technology Advanced Research, Beijing 100193, People's Republic of China

Haiyan Zheng – Center for High Pressure Science and Technology Advanced Research, Beijing 100193, People's Republic of China; orcid.org/0000-0002-4727-5912

Peijie Zhang – Center for High Pressure Science and Technology Advanced Research, Beijing 100193, People's Republic of China; orcid.org/0000-0001-6355-5482

Dexiang Gao – Center for High Pressure Science and Technology Advanced Research, Beijing 100193, People's Republic of China

Guangwei Che – Center for High Pressure Science and Technology Advanced Research, Beijing 100193, People's Republic of China

Zijia Wang – Center for High Pressure Science and Technology Advanced Research, Beijing 100193, People's Republic of China

Aijiao Guan – Institute of Chemistry, Chinese Academy of Sciences, Beijing 100190, People's Republic of China

Jun-Feng Xiang – Institute of Chemistry, Chinese Academy of Sciences, Beijing 100190, People's Republic of China; University of Chinese Academy of Sciences, Beijing 100049, People's Republic of China

Mingxue Tang – Center for High Pressure Science and Technology Advanced Research, Beijing 100193, People's Republic of China; orcid.org/0000-0002-7282-4100

Xiao Dong – Key Laboratory of Weak-Light Nonlinear Photonics and School of Physics, Nankai University, Tianjin 300071, People's Republic of China; orcid.org/0000-0003-4533-1914

Ho-kwang Mao – Center for High Pressure Science and Technology Advanced Research, Beijing 100193, People's Republic of China

Complete contact information is available at: <https://pubs.acs.org/10.1021/jacs.2c08914>

Author Contributions

The manuscript was written through contributions of all authors. All authors have given approval to the final version of the manuscript.

Notes

The authors declare no competing financial interest.

ACKNOWLEDGMENTS

The authors acknowledge the support of the National Natural Science Foundation of China (NSFC) (Grant Nos. 22022101 and 21875006). The authors also acknowledge the support of the National Key Research and Development Program of China (2019YFA0708502). This work was carried out with the support of 4W2 beamline at Beijing Synchrotron Radiation Facility and 15U1 beamline at Shanghai Synchrotron Radiation Facility. This study were also partially supported by Synergic Extreme Condition User Facility (SECUF).

REFERENCES

- (1) Ragauskas, A. J.; Williams, C. K.; Davison, B. H.; Britovsek, G.; Cairney, G.; Eckert, C. A.; Frederick, W. J.; Hallett, J.; Leak, D. J.; Liotta, C. L.; Mielenz, J. R.; Murphy, R.; Templer, R.; Tschaplinski, T. The Path forward for Biofuels and Biomaterials. *Science* **2006**, *31*, 484–489.
- (2) Zhang, J.; Li, J.; Tang, Y.; Lin, L.; Long, M. Advances in Catalytic Production of Bio-based Polyester Monomer 2,5-Furandicarboxylic Acid Derived from Lignocellulosic Biomass. *Carbohydr. Polym.* **2015**, *130*, 420–428.
- (3) Hanson, S. K.; Baker, R. T. Knocking on Wood: Base Metal Complexes as Catalysts for Selective Oxidation of Lignin Models and Extracts. *Acc. Chem. Res.* **2015**, *48*, 2037–2048.
- (4) Ma, R. S.; Xu, Y.; Zhang, X. Catalytic Oxidation of Biorefinery Lignin to Value-added Chemicals to Support Sustainable Biofuel Production. *ChemSusChem* **2015**, *8*, 24–51.
- (5) Zhang, Z.; Deng, K. Recent Advances in the Catalytic Synthesis of 2,5-Furandicarboxylic Acid and Its Derivatives. *ACS Catal.* **2015**, *5*, 6529–6544.
- (6) Zakrzewska, M. E.; Bogel-Lukasik, E.; Bogel-Lukasik, R. Ionic Liquid-Mediated Formation of 5-Hydroxymethylfurfural—a Promising Biomass-Derived Building Block. *Chem. Rev.* **2011**, *111*, 397–417.
- (7) Werpy, T.; Petersen, G.; Aden, A.; Bozell, J.; Holladay, J.; White, J.; Manheim, A. *Top Value Added Chemicals from Biomass*; U.S. Department of Energy, 2004; pp 26–28.
- (8) Rajendran, S.; Raghunathan, R.; Hevus, I.; Krishnan, R.; Ugrinov, A.; Sibi, M. P.; Webster, D. C.; Sivaguru, J. Programmed Photodegradation of Polymeric/Oligomeric Materials Derived from Renewable Bioresources. *Angew. Chem., Int. Ed.* **2015**, *54*, 1159–1163.
- (9) Wilsens, C. H. R. M.; Willems, N. J. M.; Gubbels, E.; Yao, Y. F.; Rastogi, S.; Noorder, B. A. J. Synthesis, Kinetics, and Characterization of Bio-based Thermosets Obtained through Polymerization of a 2,5-Furandicarboxylic Acid-Based Bis(2-oxazoline) with Sebacic Acid. *Polym. Chem.* **2015**, *6*, 2707–2716.
- (10) Eerhart, A. J. J. E.; Faaij, A. P. C.; Patel, M. K. Replacing Fossil based PET with Biobased PEF; Process Analysis, Energy and GHG Balance. *Energy Environ. Sci.* **2012**, *5*, 6407–6422.
- (11) Huss, S.; Wu, S.; Chen, B.; Wang, T.; Gerthoffer, M. C.; Ryan, D. J.; Smith, S. E.; Crespi, V. H.; Badding, J. V.; Elacqua, E. Scalable Synthesis of Crystalline One-Dimensional Carbon Nanotubes through Modest-Pressure Polymerization of Furan. *ACS Nano* **2021**, *15*, 4134–4143.
- (12) Matsuura, B. S.; Huss, S.; Zheng, Z.; Yuan, S.; Wang, T.; Chen, B.; Badding, J. V.; Trauner, D.; Elacqua, E.; Duin, A. C. T.; Crespi, V. H.; Schmidt-Rohr, K. Perfect and Defective ¹³C-Furan-Derived Nanotubes from Modest-Pressure Synthesis Analyzed by ¹³C NMR. *J. Am. Chem. Soc.* **2021**, *143*, 9529–9542.
- (13) Fitzgibbons, T. C.; Guthrie, M.; Xu, E. S.; Crespi, V. H.; Davidowski, S. K.; Cody, G. D.; Alem, N.; Badding, J. V. Benzene-Derived Carbon Nanotubes. *Nat. Mater.* **2015**, *14*, 43–47.
- (14) Duan, P.; Li, X.; Wang, T.; Chen, B.; Juhl, S.; Koeplinger, D.; Crespi, V. H.; Badding, J. V.; Schmidt-Rohr, K. The Chemical Structure of Carbon Nanotubes Analyzed by Advanced Solid-State NMR. *J. Am. Chem. Soc.* **2018**, *140*, 7658–7666.
- (15) Li, X.; Baldini, M.; Wang, T.; Chen, B.; Xu, E.-s.; Vermilyea, B.; Crespi, V. H.; Hoffmann, R.; Molaison, J. J.; Tulk, C. A.; Guthrie, M.; Sinogeikin, S.; Badding, J. V. Mechanochemical Synthesis of Carbon Nanotube Single Crystals. *J. Am. Chem. Soc.* **2017**, *139*, 16343–16349.
- (16) Demingos, P. G.; Muniz, A. R. Carbon Nanotubes from Polycyclic Aromatic Hydrocarbon Molecules. *Carbon* **2018**, *140*, 644–652.
- (17) Li, X.; Wang, T.; Duan, P.; Baldini, M.; Huang, H.-Y.; Chen, B.; Juhl, S. J.; Koeplinger, D.; Crespi, V. H.; Schmidt-Rohr, K.; Hoffmann, R.; Alem, N.; Guthrie, M.; Zhang, X.; Badding, J. V. Carbon Nitride Nanotube Crystals Derived from Pyridine. *J. Am. Chem. Soc.* **2018**, *140*, 4969–4972.
- (18) Biswas, A.; Ward, M. D.; Wang, T.; Zhu, L.; Huang, H.-T.; Badding, J. V.; Crespi, V. H.; Strobel, T. A. Evidence for Orientational Order in Nanotubes Derived from Thiophene. *J. Phys. Chem. Lett.* **2019**, *10*, 7164–7171.
- (19) Huang, H. T.; Zhu, L.; Ward, M. D.; Wang, T.; Chen, B.; Chaloux, B. L.; Wang, Q.; Biswas, A.; Gray, J. L.; Kuei, B.; Cody, G. D.; Epshteyn, A.; Crespi, V. H.; Badding, J. V.; Strobel, T. A. Nanoarchitecture through Strained Molecules: Cubane-Derived Scaffolds and the Smallest Carbon Nanotubes. *J. Am. Chem. Soc.* **2020**, *142*, 17944–17955.
- (20) Zhan, H. F.; Zhang, G.; Zhang, Y. Y.; Tan, V. B. C.; Bell, J. M.; Gu, Y. T. Thermal Conductivity of a New Carbon Nanotube Analog: The Diamond Nanotube. *Carbon* **2016**, *98*, 232–237.
- (21) Zhan, H.; Zhang, G.; Bell, J. M.; Tan, V. B. C.; Gu, Y. High Density Mechanical Energy Storage with Carbon Nanotube Bundle. *Nat. Commun.* **2020**, *11*, 1905.
- (22) Duan, K.; Li, Y.; Li, L.; Hu, Y.; Wang, X. Diamond Nanotube based Resonators: Ultrahigh Sensitivity and Low Dissipation. *Nanoscale* **2018**, *10*, 8058–8065.
- (23) Demingos, P. G.; Balzaretto, N. M.; Muniz, A. R. First-Principles Study of Carbon Nanotubes Derived from Five-Membered Heterocyclic Rings: Thiophene, Furan and Pyrrole. *Phys. Chem. Chem. Phys.* **2021**, *23*, 2055–2062.
- (24) Ward, M. D.; Tang, W. S.; Zhu, L.; Popov, D.; Cody, G. D.; Strobel, T. A. Controlled Single-Crystalline Polymerization of C₁₀H₈-C₁₀F₈ under Pressure. *Macromolecules* **2019**, *52*, 7557–7563.
- (25) Friedrich, A.; Collings, I. E.; Dziubek, K. F.; Fanetti, S.; Radacki, K.; Ruiz-Fuertes, J.; Pellicer-Porres, J.; Hanfland, M.; Sieh, D.; Bini, R.; Clark, S. J.; Marder, T. B. Pressure-Induced Polymerization of Polycyclic Arene-Perfluoroarene Cocrystals: Single Crystal X-ray Diffraction Studies, Reaction Kinetics, and Design of Columnar Hydrofluorocarbons. *J. Am. Chem. Soc.* **2020**, *142*, 18907–18923.
- (26) Gao, D.; Tang, X.; Xu, J.; Yang, X.; Zhang, P.; Che, G.; Wang, Y.; Chen, Y.; Gao, X.; Dong, X.; Zheng, H.; Li, K.; Mao, H.-k. Crystalline C₃N₃H₃ Tube (3,0) Nanotubes. *Proc. Natl. Acad. Sci. U.S.A.* **2022**, *119*, No. e2201165119.
- (27) Dunning, S. G.; Zhu, L.; Chen, B.; Chariton, S.; Prakapenka, V. B.; Somayazulu, M.; Strobel, T. A. Solid-State Pathway Control via Reaction-Directing Heteroatoms: Ordered Pyridazine Nanotubes through Selective Cycloaddition. *J. Am. Chem. Soc.* **2022**, *144*, 2073–2078.
- (28) Nobrega, M. M.; Teixeira-Neto, E.; Cairns, A. B.; Temperini, M. L. A.; Bini, R. One-Dimensional Diamondoid Polyaniline-Like Nanotubes from Compressed Crystal Aniline. *Chem. Sci.* **2018**, *9*, 254–260.
- (29) Wang, X.; Tang, X.; Zhang, P.; Wang, Y.; Gao, D.; Liu, J.; Hui, K.; Wang, Y.; Dong, X.; Hattori, T.; Sano-Furukawa, A.; Ikeda, K.; Miao, P.; Lin, X.; Tang, M.; Zuo, Z.; Zheng, H.; Li, K.; Mao, H.-k. Crystalline Fully Carboxylated Polyacetylene Obtained under High

Pressure as a Li-Ion Battery Anode Material. *J. Phys. Chem. Lett.* **2021**, *12*, 12055–12061.

(30) Gerthoffer, M. C.; Wu, S.; Chen, B.; Wang, T.; Huss, S.; Oburn, S. M.; Crespi, V. H.; Badding, J. V.; Elacqua, E. ‘Sacrificial’ Supramolecular Assembly and Pressure-Induced Polymerization: Toward Sequence-Defined Functionalized Nanothreads. *Chem. Sci.* **2020**, *11*, 11419–11424.

(31) Martuscelli, E.; Pedone, C. The Crystal and Molecular Structure of Furane- α,α' -Dicarboxylic Acid. *Acta Crystallogr.* **1968**, *B24*, 175–179.

(32) Ciabini, L.; Santoro, M.; Gorelli, F. A.; Bini, R.; Schettino, V.; Raugei, S. Triggering Dynamics of the High-Pressure Benzene Amorphization. *Nat. Mater.* **2007**, *6*, 39–43.

(33) Wang, Y.; Dong, X.; Tang, X.; Zheng, H.; Li, K.; Lin, X.; Fang, L.; Sun, G.; Chen, X.; Xie, L.; Bull, C. L.; Funnell, N. P.; Hattori, T.; Sano-Furukawa, A.; Chen, J.; Hensley, D. K.; Cody, G. D.; Ren, Y.; Lee, H. H.; Mao, H.-k. Pressure-Induced Diels-Alder Reactions in C_6H_6 - C_6F_6 Cocrystal towards Graphane Structure. *Angew. Chem., Int. Ed.* **2019**, *58*, 1468–1473.

(34) Li, J.; Du, Z.; Ruther, R. E.; AN, S. J.; David, L. A.; Hays, K.; Wood, M.; Phillip, N. D.; Sheng, Y.; Mao, C.; Kalnaus, S.; Daniel, C.; Wood, D. L. Toward Low-Cost, High-Energy Density, and High-Power Density Lithium-Ion Batteries. *JOM* **2017**, *69*, 1484–1496.

Recommended by ACS

Mechanochemistry of Cubane

Liqi Wang, Stephen L. Craig, *et al.*

DECEMBER 08, 2022
JOURNAL OF THE AMERICAN CHEMICAL SOCIETY

READ 

Molecular Compartments Created in Metal–Organic Frameworks for Efficient Visible-Light-Driven CO_2 Overall Conversion

Chengbin Zhao, Hexiang Deng, *et al.*

DECEMBER 15, 2022
JOURNAL OF THE AMERICAN CHEMICAL SOCIETY

READ 

Photochemically Mediated Polymerization of Molecular Furan and Pyridine: Synthesis of Nanothreads at Reduced Pressures

Shalisa M. Oburn, Elizabeth Elacqua, *et al.*

NOVEMBER 23, 2022
JOURNAL OF THE AMERICAN CHEMICAL SOCIETY

READ 

Monometallic Endohedral Azafullerene

Wenhao Xiang, Shangfeng Yang, *et al.*

NOVEMBER 10, 2022
JOURNAL OF THE AMERICAN CHEMICAL SOCIETY

READ 

Get More Suggestions >